PUBLISHED VERSION

*Zebb Prime , Akhilesh Mimani, Danielle J. Moreau and Con J. Doolan
An experimental comparison of beamforming, time-reversal and near-field acoustic holography for aeroacoustic source localization
20th AIAA/CEAS Aeroacoustics Conference, 2014 / pp.2014-2917-1-2014-2917-13

PERMISSIONS

Email reply received 28 Oct 2014 from Danielle Moreau

"Yes, I give permission for the full text of the conference publications listed* to be added to the existing Metadata in Adelaide Research & Scholarship"

28 October, 2014

http://hdl.handle.net/2440/86696

An Experimental Comparison of Beamforming, Time-reversal and Near-field Acoustic Holography for Aeroacoustic Source Localization

Zebb Prime,[*] Akhilesh Mimani,[†] Danielle J. Moreau[‡] and Con J. Doolan[§]

The University of Adelaide, South Australia, Australia 5005

Aeroacoustic source localization is an important experimental tool that uses an array of microphones to locate and quantify aeroacoustic sources. Obtaining such information is the first step towards reducing noise emissions. One emerging method of aeroacoustic source localization is aeroacoustic time-reversal. With a unique blend of numerical simulation and experimental data, aeroacoustic time-reversal has the potential to provide superior source resolution and characterization performance over other microphone array processing techniques. This paper presents an experimental comparison of three different aeroacoustic source localization methods: aeroacoustic time-reversal, beamforming and near-field acoustic holography. The source resolution performance of all three source localization methods is investigated via a wind tunnel experimental study using two line arrays of microphones for the test case of a circular cylinder in low Mach number flow. The experimental results show that all three source localization methods are able to satisfactorily locate the cylinder noise source at the aeolian tone frequency to within $\lambda/6$. In addition, information about the directivity characteristics of the noise source are obtained with aeroacoustic time-reversal and beamforming.

I.   Introduction

Microphone array techniques can be used to provide important information on the individual strength and location of aeroacoustic sources. Such knowledge is essential to reducing noise emissions. Beamforming has been successfully applied to several aeroacoustic problems in the past including wind tunnel measurements of airfoil self noise,[1] jet noise[2] and aircraft landing gear noise,[3] aircraft fly-over tests[4] and field measurements of wind turbine noise.[5] Near-field Acoustic Holography (NAH) is another common array imaging technique that has been used for aeroacoustic source localization in wind tunnel experiments.[6,7]

An alternative array processing method for localizing aeroacoustic sources is Time-Reversal (TR).[8,9] This technique promises to provide greater insight into the noise-generating physics as it is a unique blend of numerical and experimental methods and makes no assumptions about the source type. Also, as TR is performed in the time-domain, a wide variety of processing methods are available to examine the nature of the noise source. While TR has the potential to provide superior source localization to other array processing methods, there has been little experimental investigation of aeroacoustic TR in the past.

This paper presents, for the first time, an experimental comparison of three different aeroacoustic source localization methods: TR, beamforming and NAH. The source localization performance of all three methods is examined via a wind tunnel experiment using two Line Arrays (LAs) of microphones and the test case of a circular cylinder in low Mach number flow. The primary aim of this study is to compare the performance of aeroacoustic TR against the other more common source localization methods of beamforming and NAH. This paper is structured as follows: Section II provides a description of the experimental method including details of the aeroacoustic TR technique. Section III presents the experimental results including the sound maps produced with each of the source localization methods. The paper is concluded in Section IV.

---

[*]Research Associate, School of Mechanical Engineering, zebb.prime@adelaide.edu.au, AIAA member
[†]Research Associate, School of Mechanical Engineering, akhilesh.mimani@adelaide.edu.au, AIAA member
[‡]Research Associate, School of Mechanical Engineering, danielle.moreau@adelaide.edu.au, AIAA member
[§]Associate Professor, School of Mechanical Engineering, con.doolan@adelaide.edu.au, AIAA Senior member

American Institute of Aeronautics and Astronautics

II.   Experimental method

II.A.   Anechoic wind tunnel facility

Experiments have been performed in the anechoic wind tunnel at the University of Adelaide. The test chamber of this facility is 1.4 m × 1.4 m × 1.6 m (internal dimensions) and has walls that are acoustically treated with foam wedges providing a near reflection free environment above 250 Hz. The facility contains a contraction outlet that is rectangular in cross-section with dimensions of 75 mm x 275 mm. The maximum flow velocity of the free jet is ∼ 40 m/s and the free-stream turbulence intensity at the contraction outlet is 0.33%.[10] In this study, experiments have been performed at a flow speed of $U_\infty = 32$ m/s.

II.B.   Test model

The test model is a circular cylinder with diameter of 4 mm and a span of 450 mm. The cylinder is held in a two sided mounting frame that is attached to the contraction outlet, as shown in Figs. 1 and 2. The co-ordinate system is also shown in Fig. 1 where x is the streamwise direction, y is the vertical direction and z is the spanwise direction. The origin of the co-ordinate system is located at the center of the contraction outlet and the cylinder is located 50 mm downstream of the jet exit plane at $x = 50$ mm, $y = 0$.
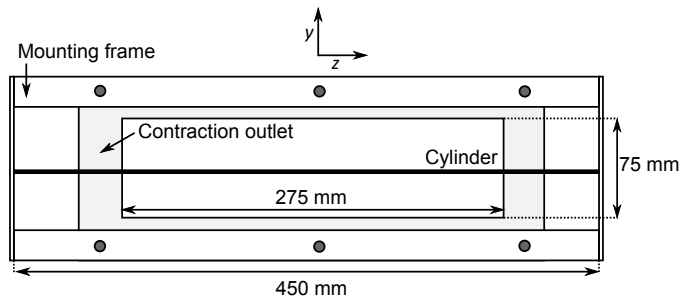

Figure 1: Schematic diagram of the circular cylinder in the mounting frame attached to the contraction outlet.

II.C.   Measurement techniques

Acoustic measurements have been taken with two LAs mounted inside the anechoic wind tunnel test chamber parallel to the flow direction, as shown in Fig. 2. Each LA consists of 32 GRAS 40PH 1/4" phase matched microphones mounted in a timber frame. The microphones are positioned with a unit to unit spacing of 30 mm so that the total length of each LA is 930 mm. For both TR and beamforming, the two LAs were positioned 700 mm apart, equidistant from the test model (at $y = 350$ mm, $z = 0$ and $y = -350$ mm, $z = 0$). For NAH, only the top LA was used and it was located parallel to the flow direction and 120 mm above the test model (at $y = 120$ mm) as shown in Fig. 3. This distance was limited by the requirement to keep the microphones out of the flow. For near-field data collection, wind socks were placed on all microphones and the LA was mounted to a Dantec automatic traverse that allowed continuous movement in the streamwise (x), vertical (y) and spanwise (z) directions. The LA was traversed in the spanwise (z) direction from the cylinder's center span at $z = 0$ to $z = -210$ mm, or to a position 72.5 mm past the edge of the contraction outlet in steps of 30 mm. This produced a regular grid of 248 measurement points above the cylinder.

The 64 array microphones are connected to a National Instruments PXI-8106 data acquisition system containing 4 PXI-4496 simultaneous sample and hold ADC cards. Data from the 64 microphones have been acquired at a sampling frequency of 2^{16} Hz for a sample time of 10 s.

II.D.   Source localization methods

II.D.1.   Aeroacoustic time-reversal

The TR results are obtained using the time-reversed experimental pressures obtained at each LA microphone as numerical sources in a computational aeroacoustics (CAA) algorithm. The CAA algorithm solved the 2D

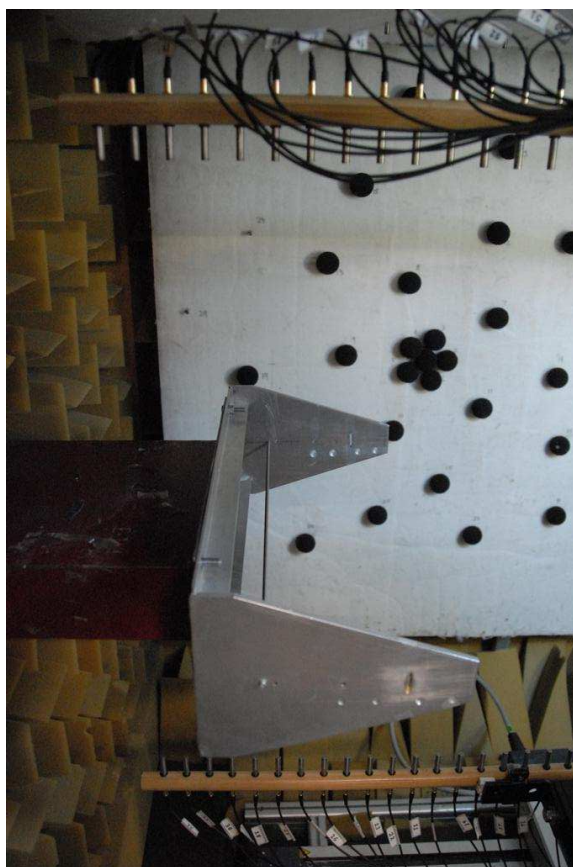American Institute of Aeronautics and Astronautics

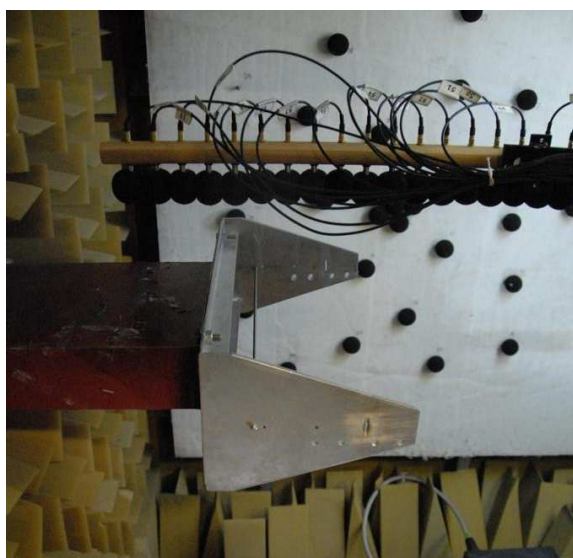Figure 2: The two LAs and the circular cylinder in the anechoic wind tunnel for far-field data collection.

Figure 3: The top LA and the circular cylinder in the anechoic wind tunnel for near-field data collection. Wind socks have been placed on all array microphones.

Linearized Euler Equations[11] (LEE) using the Pseudo-Characteristic-Formulation[12] (PCF) over the computational domain -93 mm $\leq x \leq$ 837 mm, 350 mm $\leq y \leq$ 350 mm. A stationary medium was considered in the simulation and therefore the convective effect of mean flow has been ignored. To increase the mesh resolution, the acoustic pressure signals recorded at the two LAs were interpolated using the Lagrange polynomial

American Institute of Aeronautics and Astronautics

interpolation method.[13] Two nodes were added between each pair of nodes corresponding to the microphone locations resulting in a mesh-size of $\Delta x = 10$ mm in the x direction and $\Delta y = 10$ mm in the y direction. The spatial derivatives of the acoustic pressure and acoustic particle velocities in the fluxes propagating in the opposite directions (in the PCF) were computed using an overall upwind biased Finite-Difference (FD) scheme formulated using the 4th order, 7-point optimized upwind-biased FD scheme[14] at the interior nodes and the 3rd and 5th order standard upwind-biased schemes,[15] 7-point optimized backward FD schemes[16] at the penultimate and last node of the computational boundary. The maximum frequency that may be accurately propagated on this mesh without significant dispersion error is 4.39 kHz as determined by the 3rd order standard upwind-biased FD scheme[15] which has the least Dispersion-Relation-Preserving[16,17] (DRP) characteristics amongst all of the FD schemes used. With a sampling rate of 2^{16} Hz, the sampling time is $\Delta t = 1.5259 \times 10^{-5}$ s, resulting in a CFL number of 0.53 being used in the TR simulations which is in accordance with the 3rd order Total Variation Diminishing (TVD) Runge-Kutta scheme[18] used for time-integration. The TR simulations were performed for 3×10^4 time-steps or equivalently over the time period of $\widetilde{t} = [0, 0.4577]$ s where $\widetilde{t}$ denotes the reverse time.

The time-reversed acoustic pressure history was enforced at all nodes on the two LAs after every time-step of the TR simulation. First-order CEM anechoic boundary conditions (BCs)[19] and corner BCs[20] were implemented to eliminate reflections. In addition, the acoustic flux propagating along the x direction into the computational domain from the $x = -93$ and $x = 837$ mm boundaries was damped by means of a sponge-layer to further reinforce the anechoic BCs. A Time-Reversal-Sponge-Layer (TRSL) was implemented across the first 10 nodes from (and including) the LA boundaries to minimize the deteriorating influence of spurious maxima regions caused by the interference between the opposite propagating fluxes.[9,21] The TRSL technique is based on damping the flux emanating from one of the LAs (say, at the top boundary) and propagating along the direction perpendicular towards the LA located at the opposite boundary (the bottom boundary) while leaving the outgoing fluxes propagating away from the bottom LA into the computational domain unaffected.

The location and characteristics of the aeroacoustic source in the 2D computational domain were obtained by determining the regions of maximum magnitude in the Root-Mean-Square (RMS) time-reversed acoustic pressure field[8,9,21] denoted by $\widetilde{p}_{RMS}^{TR}(x,y)$. The region(s) of maximum RMS magnitude is called a focal spot(s) and the node at which the focal spot is maximum is termed the focal point.[8,9,21] The focal point is generally coincident with the geometric center of the focal spot. The $\widetilde{p}_{RMS}^{TR}(x,y)$ field is calculated over the time-interval corresponding to when a steady-state TR acoustic field is established over the entire domain, i.e. from $\widetilde{t} = [570, 30000]\,\Delta t$. This method of localizing time-harmonic aeroacoustic sources by determining the focal spot(s) in the $\widetilde{p}_{RMS}^{TR}(x,y)$ field is based on the application of the Sommerfeld radiation condition, which states that in 2D free space, the acoustic field consists of only waves that propagate away from the source towards infinity and their amplitudes decay as $1/\sqrt{r}$ while the acoustic intensity falls as r^{-1} where r is the distance from source.[22] Therefore, the $\widetilde{p}_{RMS}^{TR}(x,y)$ field (equivalent to the acoustic intensity) is maximum at the source and the focal spot(s) yields the location of the aeroacoustic source(s). The $\widetilde{p}_{RMS}^{TR}(x,y)$ field has been converted to dB (with reference to $p_{ref} = 2 \times 10^{-5}$ Pa) and expressed relative to its magnitude at the focal point(s) given by the $\widetilde{p}_{dB}^{TR}(x,y)$ field.

II.D.2.   Beamforming

The beamforming sound maps are produced using the cross-spectral beamforming technique with diagonal removal.[23] Both monopole and dipole propagation characteristics have been used to steer the LAs.[24] The noise source distribution in the sound maps was then refined by solving the deconvolution problem using the DAMAS Gauss-Seidel iterative method,[1] allowed to run for 1000 iterations each.

II.D.3.   Near-field acoustic holography

The NAH results are obtained using planar Fourier NAH.[25,26] This source localization technique was implemented with the measurement plane located 120 mm above the cylinder and the prediction plane being 40 mm above the cylinder. An 8-point Tukey spatial window[26] was applied to the array data and zeros were added outside of the measurement area to reduce wrap-around errors. To prevent measurement noise from influencing the solution, the regularization method employed was an exponential k-space low-pass filter with a value of 0.1 for the parameter α.[26]

American Institute of Aeronautics and Astronautics

NAH was implemented assuming a stationary medium and therefore the convective effect of mean flow has been ignored. As the microphone spacing in the LA is 30 mm, the high frequency limit of NAH is $f = 5.72$ kHz. With an array position of 120 mm above the cylinder, the acoustic near-field condition of within one acoustic wavelength is obtained for frequencies below $f = 2.86$ kHz. NAH results are therefore presented for frequencies below $f = 2.86$ kHz only to ensure these frequency limits are met.

III.   Experimental results and discussion

The acoustic spectrum of the circular cylinder at a flow speed of $U_\infty = 32$ m/s is shown in Fig. 4. This spectrum was measured by the microphone located directly above the cylinder when the LAs were positioned for far-field data collection. Fig. 4 shows the cylinder produces an aeolian tone at a frequency of $f = 1.58$ kHz corresponding to a Strouhal number based on cylinder diameter of $St_D = 0.198$. Peaks are also visible in the acoustic spectrum at the second harmonic or cylinder drag dipole frequency of $f = 3.18$ kHz and at the third harmonic of $f = 4.76$ kHz. The drag dipole is recorded due to refraction effects through the shear layer.
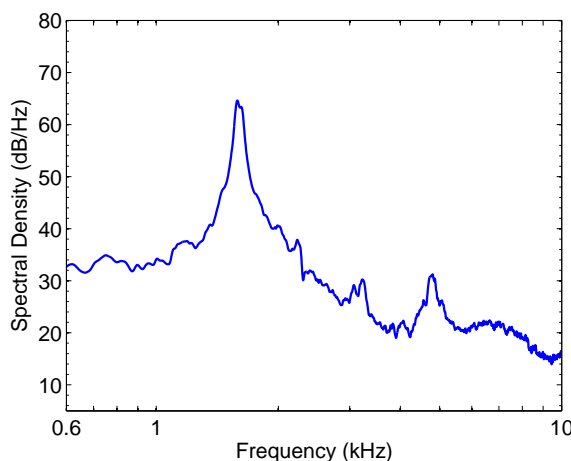

Figure 4: Acoustic spectrum of the circular cylinder at $U_\infty = 32$ m/s.

Figure 5 shows the spatial-temporal evolution of the time-reversed acoustic pressure field $\widetilde{p}(x, y, \widetilde{t})$ at the cylinder aeolian tone frequency of $f = 1.58$ kHz and $\widetilde{t} = 20\Delta t$ - $800\Delta t$ over the 2D domain obtained using the time-reversed acoustic pressure signals in the band-pass frequency range $f = [1.4, 1.8]$ kHz. As the TR results have been produced using LAs located above and below the cylinder center span, the maps in Fig. 5 are a side view in the streamwise (x) - vertical (y) plane. Figures 5 (a) and (b) show the simultaneous emission of acoustic fluxes from the top and bottom LAs, while in Fig. 5 (c), these fluxes are about to undergo constructive interference near the cylinder-axis. Figure 5 (d) shows the formation of two instantaneous focal spots of nearly the same strength but opposite phase near the cylinder-axis suggesting a dipole source. It should be noted that in this region, the width of the wave fronts have diminished while their amplitudes have significantly increased.[8, 21, 27] The opposite propagating wave fronts do not stop at the source location but propagate to the LA boundaries and this is due to the conservation of energy and also because of the absence of a time-reversed acoustic-sink.[28] Figures 5 (e) - (h) show the continuous formation of instantaneous local maxima regions (of opposite phase) in the sound field throughout the TR simulation, although the instantaneous geometric center of the two focal points slightly varies over time. Importantly, Figs. 5 (e) - (h) illustrate that implementation of the TRSL[9, 21] gradually absorbs or damps the normally incident acoustic flux on the LAs, therefore preventing interference between the opposing fluxes near the LA boundaries. This suppresses the formation of spurious local maxima and prevents them from spreading in the computational domain. Use of the TRSL damping therefore ensures a high quality TR simulation.

Figure 6 shows the source localization results obtained with aeroacoustic TR at $f = 1.58$ kHz corresponding to the aeolian tone or cylinder lift dipole frequency. The sound map in Fig. 6 shows the RMS of the $\widetilde{p}(x, y, \widetilde{t})$ field (expressed in dB relative to the focal points) and has been obtained using the band-passed time-reversed acoustic pressure in the frequency range of $f = [1.4, 1.8]$ kHz. The TR sound map displays two focal spots above and below the cylinder location indicating the existence of a dipole type aeroacoustic
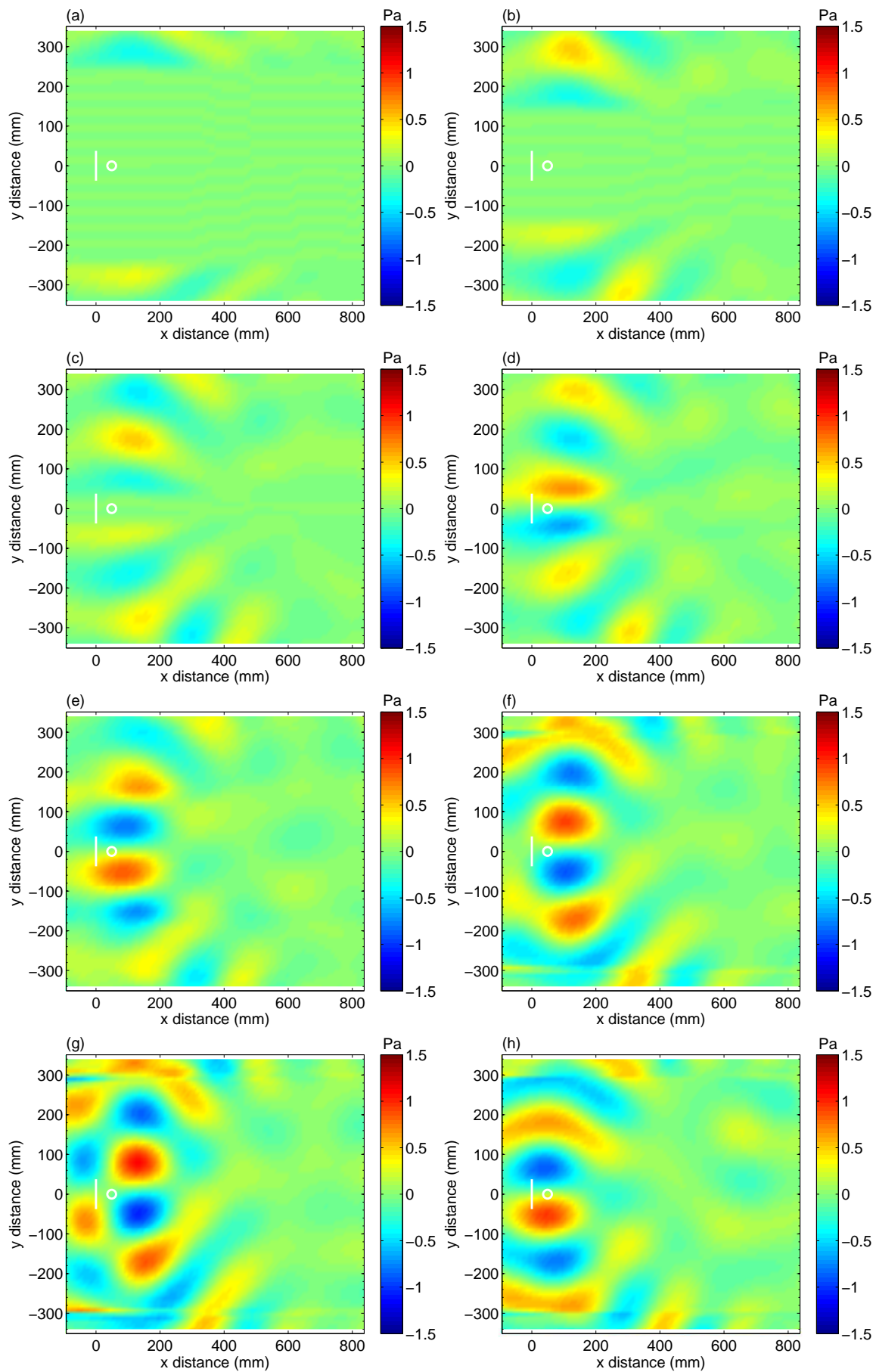
American Institute of Aeronautics and Astronautics

Figure 5: Spatial-temporal evolution of the time-reversed acoustic pressure field at $f = 1.58\,\mathrm{kHz}$ for $\widetilde{t}$ of (a) $20\Delta t$, (b) $40\Delta t$, (c) $60\Delta t$, (d) $80\Delta t$, (e) $100\Delta t$, (f) $200\Delta t$, (g) $400\Delta t$ and (h) $800\Delta t$. The contraction outlet, LAs and cylinder location are shown in white.
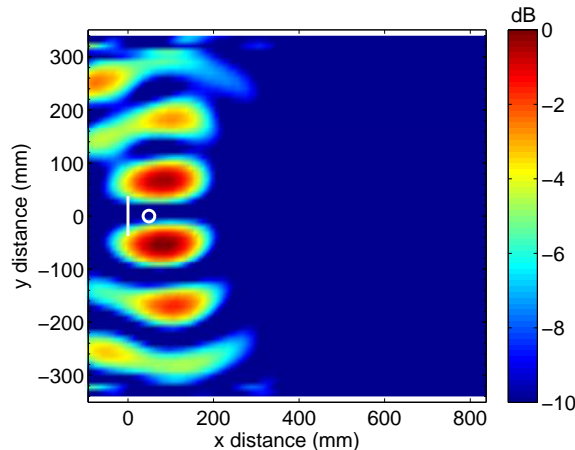
American Institute of Aeronautics and Astronautics

Figure 6: Sound map for the circular cylinder produced with aeroacoustic TR at $f = 1.58\,\text{kHz}$. The contraction outlet, LAs and cylinder location are shown in white.

source. The location of the focal points is given in Table 1. The predicted location of the dipole source is taken as the geometric center of the two focal points and is given by $x = 87$ mm, $y = 10$ mm. The TR simulation (assuming a stationary medium) can therefore localize the sound source to within a distance of $\lambda/6$ of the true cylinder location. The accuracy of the predicted source location can however, be significantly improved by incorporating the convective effect of mean flow in the 2D LEE during the aeroacoustic TR simulation.

Table 1: Locations of the dominant focal spots in the sound maps. The true cylinder location is $(x,\,y) = (50,\,0)$ mm.

Method	$f = 1.58$ kHz, $(x,\,y)$ mm	$f = 3.17$ kHz, $(x,\,y)$ mm
Aeroacoustic TR	(87, -50), (87, 70)	(127, -60), (127, 9), (12, 9)
Monopole BF	(69.9, -54.4), (66.7, 70.4)	(124.3, -64), (121.1, 6.4), (25.1, 12.8)
Monopole DAMAS	(90.4, 65.5)	(123, -65.3), (128.5, 16.3), (25.1, 10.9)
Dipole BF	(66.7,9.6)	(162.7,-64), (159.5,12.8), (82.7,16), (85.9,-67.2)
Dipole DAMAS	(57.7,10.9)	(161.1,-65.3), (74.1,10.9), (161,10.9), (74,-65)
NAH	(77.5, −)	−

The temporal evolution of the time-reversed acoustic pressure field at the predicted lift dipole location and the top and bottom focal points is shown in Fig. 7 over the reverse time-interval $\widetilde{t} = [0,\,0.28]$ s. Figure 7 demonstrates amplitude modulation is visible in the time-reversed acoustic pressure history at these locations. The acoustic pressure variation at the predicted dipole location is related to the total fluctuating lift force experienced by the cylinder in cross-flow. Moreover, Figs. 7 (b) and (c) show that the time-reversed acoustic pressure history at the top and bottom focal points are nearly in opposite phase, while the maximum magnitude of the acoustic pressure is minimum at the predicted source location, thereby indicating a dipole sound source.

Figure 8 shows the source localization results obtained with aeroacoustic TR at the cylinder drag dipole frequency of $f = 3.17$ kHz. The sound map in Fig. 8 shows the RMS of the $\widetilde{p}(x,y,\widetilde{t})$ field obtained using the band-passed time-reversed acoustic pressure in the frequency range of $f = [2.95, 3.35]$ kHz. Table 1 states the location of the focal spots in the sound map. While it is difficult to discern the exact noise source location from the sound map of Fig. 8, the focal spot pattern suggests the dominant sound source is dipolar in nature. At the drag dipole frequency however, the dipole axis should be orientated parallel to the flow direction. The focal spot pattern of Fig. 8 does not display the expected drag dipole source nature and this can be attributed to the reflection of acoustic waves at the contraction outlet or the fact that reflecting boundary conditions were not modeled at the contraction outlet during the TR simulation. It is also possible that considering the third dimension (the z direction) and implementing a 3D TR simulation and also reorienting
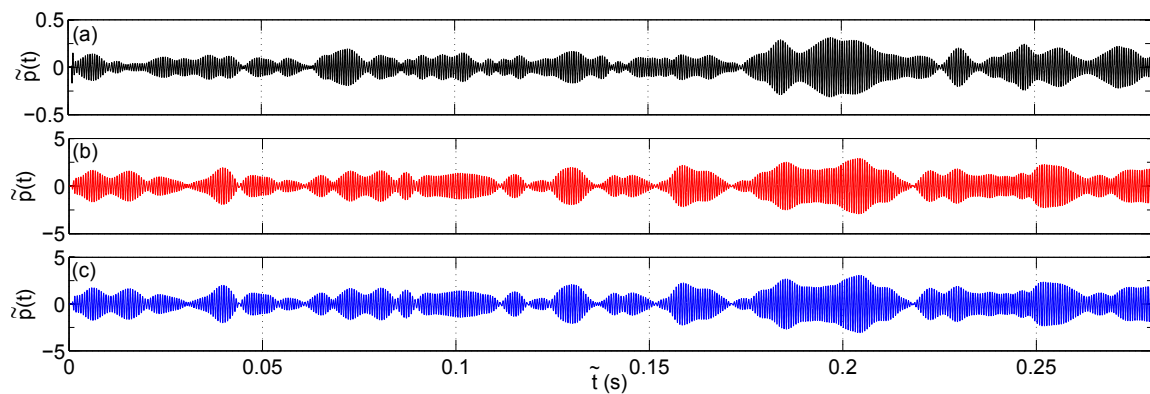
American Institute of Aeronautics and Astronautics

Figure 7: Temporal evolution of the acoustic pressure field at (a) the predicted dipole location, (b) the top focal point and (c) the bottom focal point.
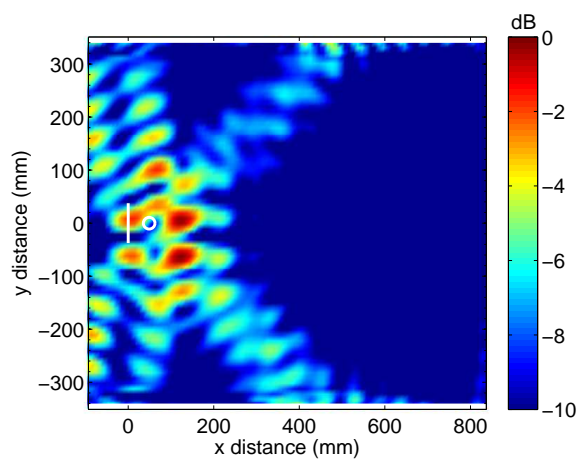

Figure 8: Sound map for the circular cylinder produced with aeroacoustic TR at $f = 3.17\,\text{kHz}$. The contraction outlet, LAs and cylinder location are shown in white.

American Institute of Aeronautics and Astronautics

the direction of one of the LAs along the cylinder-axis (z direction) may result in better resolution of the drag dipole.

Figures 9 and 10 show the source localization results obtained with beamforming at frequencies corresponding to the cylinder lift and drag dipole of $f = 1.58$ and 3.17 kHz, respectively. The beamforming sound maps have been produced using LAs located above and below the cylinder center span and so are a side view in the streamwise (x) - vertical (y) plane.

The sound map obtained with monopolar beamforming in Fig. 9 (a) is highly comparable to that produced with aeroacoustic TR at the cylinder lift dipole frequency (see Fig. 6). Both source localization methods show two focal spots equi-distant from the cylinder aligned in the vertical direction. The locations of the two focal spots in the monopolar beamforming sound map of Fig.9 (a) are given in Table 1. The geometric center of the focal spots and the predicted location of the noise source is $x = 66.8$ m, $y = 8$ mm. Monopolar beamforming therefore predicts the noise source to within $\lambda/12$ of the true cylinder location.

The dipolar directivity of the noise source at the cylinder lift dipole frequency is confirmed by examining the sound map produced with dipolar beamforming in Fig. 10 (a) which shows a single focal spot located close to the cylinder. The position of this focal spot is given in Table 1 and corresponds to a predicted source location of $\lambda/13$ from the true cylinder location.

Figure 9 (b) and Table 1 show that applying deconvolution to the monopolar beamforming result at the cylinder lift dipole frequency results in poorer prediction of the noise source location at a position of $\lambda/3$ from the true cylinder location. Conversely, deconvolution with dipolar beamforming accurately predicts the noise source location to be within $\lambda/24$ of the true cylinder location at the lift dipole frequency (see Fig. 10 (b)).

At the drag dipole frequency, the sound maps produced with beamforming in Figs. 9 (c) and (d) and 10 (c) and (d) display a complex focal spot pattern with the location of the dominant focal spots given in Table 1. While it is difficult to discern the exact noise source location from the sound maps, the focal spot patterns do indicate that the dominant noise source is dipolar in nature. Similar to aeroacoustic TR, the focal spots are however, not oriented parallel to the flow and therefore do not exhibit the expected drag dipole nature of the cylinder noise source.

Figure 11 shows the sound map obtained with NAH at the cylinder aeolian tone frequency of $f = 1.58$ kHz. Results for NAH are presented at this frequency only to ensure the near-field acoustic condition is maintained. As NAH produces a sound map that is parallel to the measured surface, the sound map in Fig. 11 is a top view in the streamwise (x) - spanwise (z) plane. It is also important to note that as the measurement plane encompassed half of the cylinder span only, the sound map has been mirrored about the cylinder's center span.

The sound map produced with NAH in Fig. 11 shows a large focal spot distributed along the cylinder's span with dominant noise radiation occurring from the cylinder's mid region. The center of the dominant focal spot location is given in Table 1 and the noise source is predicted to be at a position of $\lambda/8$ downstream of the true cylinder location. The downstream offset in the predicted noise source location is likely due to the fact that the effect of mean flow convection has been ignored in this source localization method. With the LA configuration used in near-field data collection, no information could be gained about the directivity of the noise source with NAH.
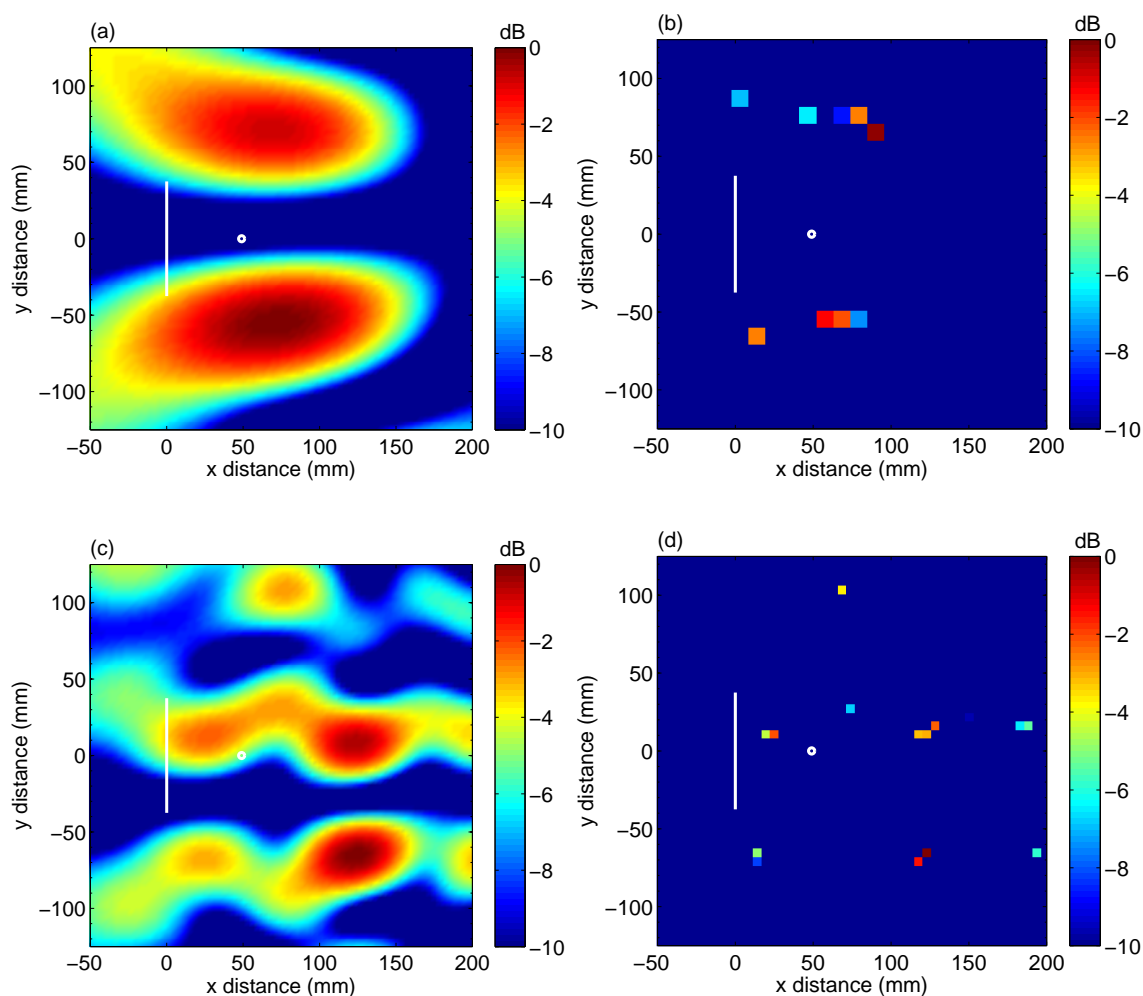
American Institute of Aeronautics and Astronautics

Figure 9: Sound maps for the circular cylinder produced with monopolar beamforming. (a) Monopole BF, $f = 1.58\,\text{kHz}$, (b) monopole DAMAS, $f = 1.58\,\text{kHz}$, (c) monopole BF, $f = 3.18\,\text{kHz}$ and (d) monopole DAMAS, $f = 3.18\,\text{kHz}$. The contraction outlet and cylinder location are shown in white.

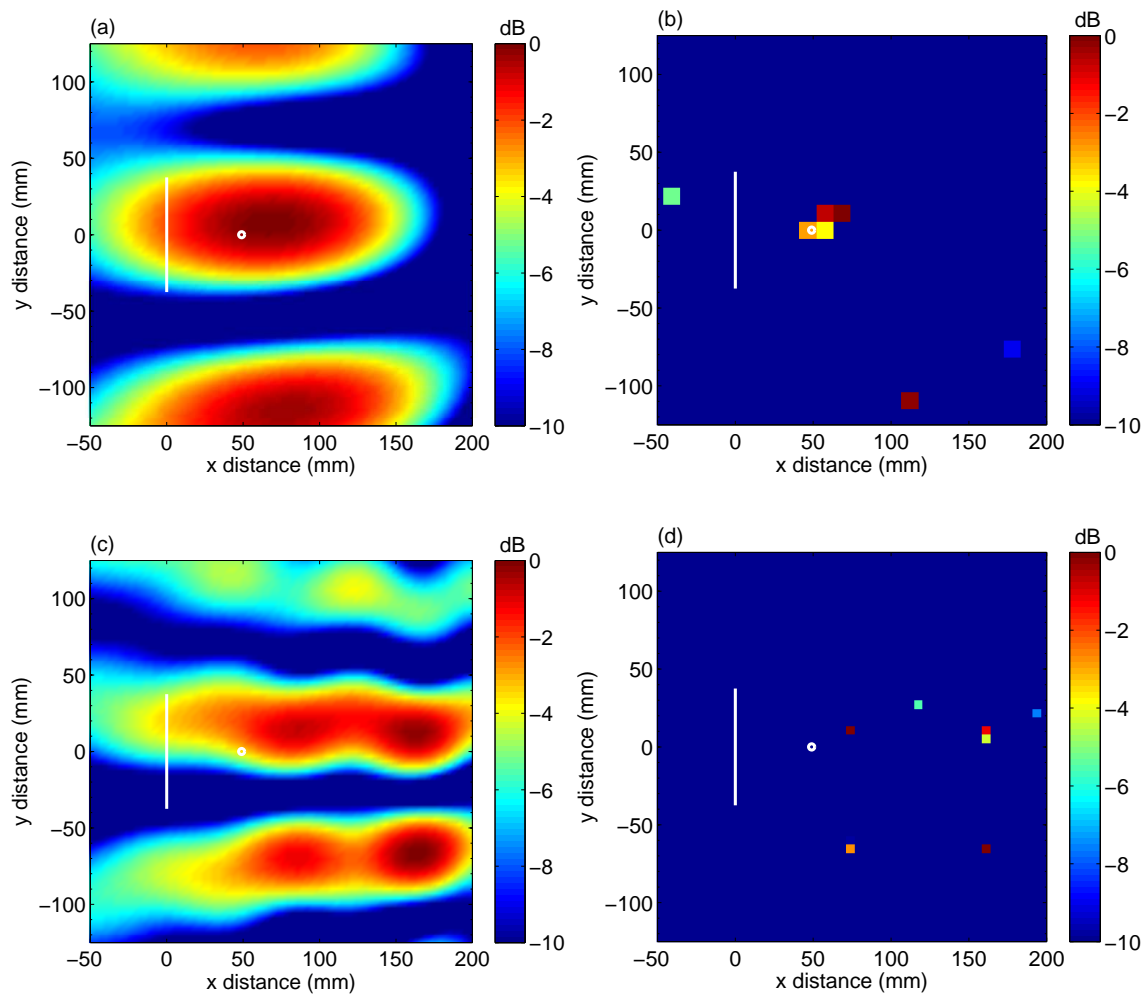American Institute of Aeronautics and Astronautics

Figure 10: Sound maps for the circular cylinder produced with dipolar beamforming. (a) Dipole BF, $f = 1.58\,\mathrm{kHz}$, (b) dipole DAMAS, $f = 1.58\,\mathrm{kHz}$, (c) dipole BF, $f = 3.18\,\mathrm{kHz}$ and (d) dipole DAMAS, $f = 3.18\,\mathrm{kHz}$. The contraction outlet and cylinder location are shown in white.
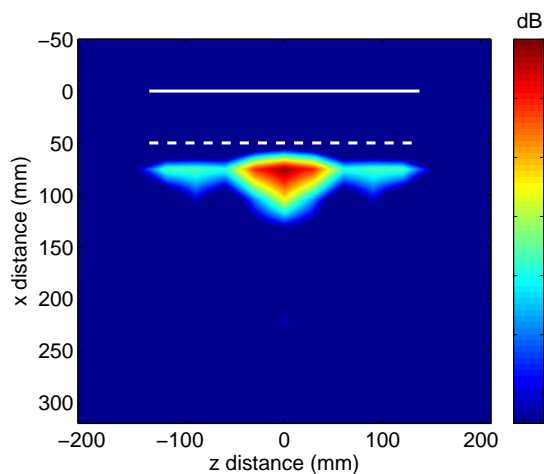

Figure 11: Sound map produced with NAH on a reconstruction plane 40 mm above the circular cylinder at $f = 1.58\,\mathrm{kHz}$. The contraction outlet is shown as a solid white line and the cylinder location is shown as a dashed white line.

American Institute of Aeronautics and Astronautics

IV.   Conclusion

This paper has presented an experimental comparison of aeroacoustic TR, beamforming and NAH for aeroacoustic source localization. The performance of all three methods has been investigated for the test case of a circular cylinder in low Mach number flow. The experimental results have shown that all three source localization methods are able to satisfactorily locate the cylinder noise source at the aeolian tone or cylinder lift dipole frequency of $f = 1.58$ kHz to within $\lambda/6$, $\lambda/24$ and $\lambda/8$ (in the streamwise direction only) for aeroacoustic TR (assuming a stationary medium), beamforming and NAH (assuming a stationary medium), respectively. In addition, the dipolar nature of the noise source is evident in the sound maps produced with aeroacoustic TR and beamforming. No information about the directivity characteristics of the noise source could be obtained with NAH due to the LA configuration used in near-field data collection. At the cylinder drag dipole frequency of $f = 3.17$ kHz, neither aeroacoustic TR or beamforming clearly locate the noise source or capture its expected directivity characteristics but this is possibly due to the LA configuration used in this experiment or the fact that the reflection of acoustic waves and the reflecting boundary conditions at the contraction outlet were not modeled during the TR simulation.

Acknowledgments

References

[1]Brooks, T.F. and Humphreys, W.M. Jr, "A Deconvolution Approach for the Mapping of Acoustic Sources (DAMAS) determined from phased microphone arrays", *Journal of Sound and Vibration* 294 (2006) 856 – 879.

[2]Suzuki, T. "Identification of multipole noise sources in low Mach number jets near the peak frequency", *Journal of the Acoustical Society of America* 119(6) (2006) 3649 – 3659.

[3]Dobrzynski, W., Ewert, R., Pott-Pollenske, M., Herr, M.and Delfs, J. "Research at DLR towards airframe noise prediction and reduction", *Aerospace Science and Technology* 12 (2008) 80 – 90.

[4]Hald, J., Ishii, Y., Ishii, T., Oinuma, H., Nagai, K., Yokokawa, Y. and Yamamoto, K. "High-resolution fly-over beamforming using a small practical array", Proceedings of the 18th AIAA/CEAS Aeroacoustics Conference, AIAA Paper 2012 – 2229, Colorado Springs, CO, 4 – 6 June 2012.

[5]Oerlemanns, S., Fisher, M., Maeder, T. And Kgler, K. "Reduction of wind turbine noise using optimized airfoils and trailing-edge serrations", *AIAA Journal* 47(6) (2009).

[6]Faszer, A.C., Hynes, T.P., Blaabjerg, C. and Shin, H-C. "Acoustic beamforming and holography measurements of modified boundary layer trailing-edge noise", Proceedings of the 12th AIAA/CEAS Aeroacoustics Conference, AIAA Paper 2006 – 2566, Cambridge, MA, 8 – 10 May 2006.

[7]Parisot-Dupuis, H., Simon, F. and Piot, E. "Nearfield acoustic holography in wind tunnel by means of velocity LDV measurements", Proceedings of Acoustics 2012, Nantes, France, 23 – 27 April 2012.

[8]Padois, T., Prax, C., Valeau, V. and Marx, D., "Experimental localization of an acoustic sound source in a wind-tunnel flow by using a numerical time-reversal technique", *Journal of the Acoustical Society of America* 132(4) (2012) 2397 – 2407.

[9]Mimani., A., Doolan, C. J., and Medwell, P.R., "Multiple line arrays for the characterization of aeroacoustic sources using a time-reversal method", *Journal of the Acoustical Society of America* 134(4) (2013) EL327 – EL333.

[10]Moreau, D.J., Brooks, L.A. and Doolan, C.J. "Broadband trailing edge noise from a sharp-edged strut", *Journal of the Acoustical Society of America* 129(5) (2011) 2820 – 2829.

[11]Bailly, C. and Juve, D., "Numerical solution of acoustic wave propagation problems using linearized Euler equations", *AIAA Journal* 38(1) (2000) 22–29.

[12]Sesterhenn, J., "A characteristic-type formulation of the Navier-Stokes equations for high order upwind schemes", *Computers and Fluids* 30(1) (2001) 37–67.

[13]Atkinson, K.E., *An introduction to numerical analysis*, 2nd ed., John Wiley & Sons, Singapore, 2004.

[14]Zhuang, M. and Chen, R. F. "Applications of high-order optimized upwind schemes for computational aeroacoustics", *AIAA Journal* 40(3) (2002) 443 – 449.

[15]Li, Y. "Wavenumber-extended high-order upwind-biased finite difference schemes for convective scalar transport", *Journal of Computational Physics* 133(2) (1997) 235 – 255.

[16]Tam, C. K. W. "Computational aeroacoustics: issues and methods", *AIAA Journal* 33(10) (1995) 1788 – 1796.

[17]Tam, C.K.W. and Webb, J.C. "Dispersion-relation-preserving finite-difference schemes for computational acoustics", *Journal of Computational Physics* 107(2) (1993) 262 – 281.

[18]Gottlieb, S. and Shu, C-W. "Total variation diminishing Runge-Kutta schemes", *Mathematics of Computation* 67(221) (1998) 73 – 85.

[19]Clayton, R. and Engquist, B. "Absorbing boundary conditions for acoustic and elastic wave equations", *Bulletin of Seismological Society of America* 67(6) (1977) 1529 – 1540.

[20]Engquist, B. and Majda, A. "Radiation boundary conditions for acoustic and elastic wave calculations", *Communications in Pure and Applied Mathematics* 32(3) (1979) 313 – 357.

American Institute of Aeronautics and Astronautics

[21]Mimani, A., Prime, Z., Doolan, C.J., and Medwell, P.R. "A sponge-layer damping technique for aeroacoustic time-reversal", submitted to the Journal of Sound and Vibration (2014).

[22]Sommerfeld, A. *Partial Differential Equations in Physics*, Academic Press, New York, 1964.

[23]Underbrink, J.R., *Aeroacoustic Measurements*, Springer, Berlin, 2002.

[24]Liu, Y., Quayle, A.R. and Dowling A.P., "Beamforming correction for dipole measurement using two-dimensional microphone arrays", *Journal of the Acoustical Society of America* 124(1) (2008) 182–191.

[25]Maynard, J.D., Williams, E.G. and Lee, Y. "Nearfield acoustic holography. I. Theory of generalized holography and the development of NAH", *Journal of the Acoustical Society of America* 78 (1985) 1395 – 1413.

[26]Williams, E.G., *Fourier Acoustics: Sound Radiation and Nearfield Acoustical Holography*, Academic Press, San Diego, 1999.

[27]Mimani. A., Doolan, C.J., and Medwell, P.R. "Localization of a stationary time-harmonic dipole sound source in flows using time-reversal simulation", Proceedings of Acoustics 2013, Victor Harbor, Australia, 17 – 20 November 2013.

[28]Rosny, J. and Fink, M. "Overcoming the diffraction limit in wave physics using a time-reversal mirror and a novel acoustic sink", *Physical Review Letters* 89(12) (2002) 12430111243014.

American Institute of Aeronautics and Astronautics